Asian Journal of Pharmaceutical Sciences 17 (2022) 751–766

Available online at www.sciencedirect.com

ScienceDirect

journal homepage: www.elsevier.com/locate/AJPS

Original Research Paper

Ferroptosis-induced anticancer effect of resveratrol with a biomimetic nano-delivery system in colorectal cancer treatment

Ziting Zhang[a,1], *You Ji*[b,1], *Nan Hu*[c,1], *Qinqi Yu*[a], *Xinrui Zhang*[a], *Jie Li*[a], *Fenglei Wu*[c,*], *Huae Xu*[b,*], *Qiyun Tang*[a,*], *Xiaolin Li*[a,*]

[a] *Department of Geriatric Gastroenterology, the First Affiliated Hospital of Nanjing Medical University, Nanjing 210009, China*
[b] *Department of Pharmaceutics, School of Pharmacy, Nanjing Medical University, Nanjing 211166, China*
[c] *Department of Oncology, the Affiliated Hospital of Kangda College of Nanjing Medical University & the First People's Hospital of Lianyungang, Lianyungang 222000, China*

ARTICLE INFO

Article history:
Received 15 May 2022
Revised 27 June 2022
Accepted 31 July 2022
Available online 22 September 2022

Keywords:
Resveratrol
Red-blood-cell membrane
Colorectal cancer
Ferroptosis
IRGD

ABSTRACT

Ferroptosis is a novel form of programmed cell death impelled by iron-dependent lipid peroxidation, which may be a potential strategy for cancer therapy. Here we demonstrated for the first time that Resveratrol (RSV), a traditional Chinese medicine (TCM) chemical monomer, could effectually inhibit the growth of colon cancer cells through the ROS-dependent ferroptosis pathway. Mechanistically, RSV evoked the increase of reactive oxygen species and lipid peroxidation in colorectal cancer cells, and eventually lead to ferroptosis. Furthermore, RSV could promote ferroptosis by downregulating the expression of the channel protein solute carrier family 7 member 11 (SLC7A11) and glutathione peroxidase 4 (GPX4). To improve the delivery efficiency of RSV, a biomimetic nanocarrier was developed by coating RSV-loaded poly(ε-caprolactone)–poly(ethylene glycol) (PCL-PEG) nanoparticles with erythrocyte membrane (RSV-NPs@RBCm). The RSV-NPs@RBCm provide the possibility to escape macrophage phagocytosis and have a long circulation effect. In addition, when coupled with a tumor-penetrating peptide iRGD, which could trigger enhanced tissue penetration tumor-specifically, the delivery of RSV-NPs@RBCm into tumors would be significantly improved results from the *in vivo* study demonstrated an excellent treatment efficacy for CRC. Altogether, our study highlighted the therapeutic potential of RSV as a ferroptosis-inducing anticancer agent and when loaded into a biomimetic nanoplatform, it might pave the way for the application of RSV loaded nanosystems for colorectal cancer treatment.

* Corresponding authors.
E-mail addresses: wufenglei1981@163.com (F. Wu), xuhuae@njmu.edu.cn (H. Xu), tqy831@163.com (Q. Tang), lxl@njmu.edu.cn (X. Li).
[1] These authors contributed equally to this work.
Peer review under responsibility of Shenyang Pharmaceutical University.

https://doi.org/10.1016/j.ajps.2022.07.006

1. Introduction

Colorectal cancer is the third leading cause of death among all cancers with the death of nearly 900,000 each year [1,2]. Chemotherapy is still the main treatment for colorectal cancer to delay tumor growth and improve life expectancy in addition to surgery, while its low specificity often leads to severe toxicity [3]. Therefore, there is an active demand to explore novel treatments with low toxicity for the treatment of colorectal cancer.

Ferroptosis is the most recently discovered nonautophagic and nonapoptotic programmed cell death that depends on iron and reactive oxygen species (ROS) [4,5]. It results in the increment of lipid peroxidation products, which in turn leads to the destruction of cell structure and integrity [6]. It is mainly characterized morphologically by cytological changes, including mitochondrial reduction, mitochondrial membrane thickening, and reduction or even disappearance of the mitochondrial ridge [7]. This process is triggered by iron overload, lipid peroxidation, increased ROS levels, and decreased glutathione (GSH) levels [8,9]. In ferroptosis, the accumulation of oxidative products (especially phospholipid hydroperoxides) and lethal ROS derived from iron metabolism is considered a symbol of ferroptosis [10]. Dixon et al. confirmed that the formation of iron-dependent ROS and lipid oxidation were related to ferroptotic cell death [9]. Induction of ferroptosis is emerging as one of the most effective ways to suppress cancer.

In recent years, more and more traditional Chinese medicine (TCM) chemical monomers have become a hot spot for CRC treatment research due to their irreplaceable advantages of chemotherapy drugs [11,12]. Resveratrol (RSV) is a kind of TCM chemical monomer, which can play a therapeutic role through "multi-target, multi-mechanism, and multi-organ" [13,14]. Current studies have demonstrated that RSV can play an anti-tumor role in cancer [15]. It has been suggested in the paper that the anti-cancer mechanism of RSV may be through targeting the metabolism of tumor cells, promoting the overload of the mitochondrial electron transport chain, and finally augmenting the production of ROS [13]. Du et al. also demonstrated that RSV inhibits cancer cell proliferation by elevating intracellular ROS levels [15]. While the characteristics of ferroptosis are an imbalance of iron metabolism and the increment of intracellular lipid ROS [16]. These findings indicate that RSV may take part in causing tumor cell death through ferroptosis. In our study, we confirmed for the first time that ferroptosis brought about RSV-induced cell death in colorectal cancer associated with ROS accumulation, lipid peroxidation, and SLC7A11 downregulation. Despite these potential findings regarding the anticancer effects of RSV, its application *in vivo* is greatly limited owing to its poor water solubility and low bioavailability [17].

One of the feasible solutions to solve the poor water solubility of drugs is to prepare them as nanomedicines. Traditionally, the most common approach has been to modify the surface of nanoparticles with synthetic polymer poly(ethylene glycol) (PEG) [18,19]. However, PEGylation is also associated with a negative effect of the "PEG dilemma", so it is hard for drugs to be absorbed by cells and then escape from endosomes [20,21]. Moreover, multiple administrations of PEGylated nanocarriers will result in the accelerated blood clearance (ABC) phenomenon [22,23]. Therefore, more effective nano-drug delivery strategies are needed to conquer the problems associated with the use of PEGylation. Nowadays, there have been appreciable achievements devoted to bionic nanotechnology, especially cell membrane coating nanotechnology [24]. The resulting cell membrane-coated nanocarriers intrinsically imitate the characteristics of their membrane-derived source cells [25]. Among them, erythrocytes are very favorable for extraction and purification as drug carriers due to their large number, long blood circulation time, the abundant "self-markers" on the surfaces, and lack of nucleus and organelles in mature erythrocytes [26]. Erythrocytes are very favorable for extraction and purification as drug carriers due to their large number, long blood circulation time, and lack of nucleus and organelles in mature erythrocytes [27]. Thus, the erythrocyte membrane-coated nanoparticles possess many progressive properties, such as favorable biocompatibility and biodegradability, long-term circulation time, immune escape ability, and easy manufacture [28]. Despite these above advantages, all the current erythrocyte membrane-coated nano-drug delivery systems are still limited by the lack of active targeting capacity, which hinders the deep penetration into the solid tumors.

Common nano-drug delivery systems achieve passive targeting of tumors by way of the enhanced permeability and retention (EPR) effect, whereas the vasculature of solid tumors may vary by tumor type, making the EPR effect in tumors highly alterable [29,30]. The repeated occurrence of the low EPR effect results in inadequate accumulation of nanoparticles in solid tumors [31]. To improve the tumor specificity and penetration, nanoparticles have been vastly decorated with tumor-homing ligands [32]. Research shows that the tumor-penetrating peptide iRGD could improve the accumulation of nanocarriers within solid tumors overexpressing $\alpha v\beta 3$ integrin and neuropilin-1 (NRP-1) [33]. iRGD is often used for membrane modification in bionic drug delivery systems, but this covalent conjugation strategy carries the risk of affecting phospholipid bilayers as well as membrane proteins [34]. It has been reported that enhanced tumor-targeting and tissue-penetrating activity could be achieved when the nanocarriers were co-administered with iRGD [35]. Inspired by this idea, we constructed a kind of biomimetic nanoparticles that enhanced the efficacy of RSV-induced ferroptosis. At the same time, co-delivery of iRGD enhanced the anti-tumor effect of the system *in vivo*. This design may promote the development of smart nanomedicine for colorectal cancer therapy.

2. Materials and methods

2.1. *Materials*

Resveratrol (RSV, ≥98.0%) and Coumarin-6 (C6, ≥98.0%) were purchased from Aladdin Biochemical Technology (Shanghai, China). mPEG5K-PCL20K was got from Ruixi (Xi'an,

China). RIPA lysis buffer and skimmed milk powder were got from Epizyme (Shanghai, China). Malondialdehyde (MDA) assay, SLC7A11/xCT Rabbit Polyclonal Antibody, GPX4 Rabbit Polyclonal Antibody, and 3-(4,5-dimethyl-2-thiazolyl)-2,5-diphenyl-2-H-tetrazolium bromide (MTT) were obtained from Beyotime (Nanjing, China). Reactive oxygen species assay kit and JC-1 mitochondrial membrane potential assay kit were got from Yeasen Biotechnology (Shanghai, China). DAPI was obtained from Fcmacs Biotech (Nanjing, China). RPMI1640 and Fetal bovine serum (FBS) were got from Biological Industries (Israel).

2.2. Cancer cell lines and experimental animals

Human colorectal cancer cell lines HT29 and HCT116 cell lines were achieved from the National Collection of Authenticated Cell Cultures. Cells culture conditions were RPMI1640 with 10% FBS and 1% penicillin/streptomycin. SPF-grade C57/BL6j, female nude mice aged 6 weeks were obtained from the animal center of Nanjing Medical University. All mice were reared in SPF environments at 23 °C. All animal experiment procedures were permitted by the institution's animal subject review committee (IACUC-2104050).

2.3. Preparation of RSV-NPs@RBCm

2.3.1. Preparation of nanoparticles

mPEG5K-PCL20K (5 mg) and RSV (1 mg) were dissolved in 1 ml acetone, and the above solution was dropped in the stirred ultrapure water. The obtained solution was placed in a dialysis bag to completely remove methanol by dialysis. C6 was loaded in the nanoparticles in the same way and C6 loaded nanoparticles (C6-NPs) were obtained. Finally, the RSV-loaded nanoparticles and the drug-free nanoparticles were added with appropriate amounts of poloxamer 188 as a lyophilization protectant and freeze-dried for the next experiments.

2.3.2. Extraction and separation of erythrocyte membranes

Fresh whole blood was obtained from C57/BL6j mice and then centrifuged (800 g, 5 min, 4 °C) to remove all components except red blood cells. The obtained erythrocytes were rinsed 3 times with phosphate-buffered saline (PBS) and then hypotonic lysed with low permeability of PBS for 40 min. The lysed hemoglobin was cleared by centrifugation at 7000 g (15 min, 4 °C). Repeated lysis is performed 2-3 times. Then repeatedly freeze-thaw to obtain pink or white red blood cell membrane. The erythrocyte membranes were stored at −80 °C.

2.3.3. Preparation of biomimetic nanoparticles on erythrocyte membrane

The erythrocyte membranes prepared in 2.3.2 were ultrasonicated in ice water for 4 min, and then the supernatant erythrocyte membrane vesicles were removed by centrifugation. The erythrocyte membrane vesicles were mixed with the nanoparticles prepared in 2.3.1 and sonicated in the ice water for 20–30 min. The erythrocyte membrane-coated C6-NPs (R-C6-NPs) were prepared as described above.

2.4. Characterization of RSV-NPs@RBCm

The morphology of nanospheres and RSV-NPs@RBCm was characterized by transmission electron microscopy (TEM). The particle size and potential of both were measured by dynamic light scattering spectroscopy (DLS) before freeze-drying. Proteins in RBCm and RSV-NPs@RBCm were characterized by 10% sodium dodecyl sulfate-polyacrylamide gel electrophoresis (SDS-PAGE), and the resultant gels were stained in coomassie brilliant blue for visualization.

2.5. Drug loading content (DLC) and encapsulation efficiency (EE)

The DLC and EE of RSV were detected by HPLC. The instruments were Shimadzu LC-10AD (Shimadzu, Japan) HPLC. The mobile phase of RSV was methanol/bis-distilled water (60/40, v/v) at a flow rate of 1.0 ml/min with a detection wavelength of 306 nm. The DLC and EE were reckoned with by the Eq. 1 and 2, respectively.

$$\text{DLC}\ (\%) = (\text{weight of the drug in nanospheres} \div \text{total weight of the nanospheres}) \times 100\% \quad (1)$$

$$\text{EE}\ (\%) = (\text{weight of the drug in nanospheres} \div \text{weight of the feeding drugs}) \times 100\% \quad (2)$$

2.6. In vitro release

10 mg RSV-NPs or RSV-NPs@RBCm were dissolved in 1 ml PBS (PH 7.4). These solutions were put in the dialysis bag respectively and added to 80 ml PBS release medium with pH 7.4 or 6.5 at 37 °C with stirring to investigate the release. At 1, 2, 4, 6, 8, 12, 24 and 48 h, 1 ml the release medium was taken, and added 1 ml fresh PBS. The peak area was measured by HPLC to calculate the amount of RSV released at each time point.

2.7. In vitro stability

4 mg RSV-NPs or RSV-NPs@RBCm were dissolved in 2 ml phosphate-buffered saline and fetal bovine serum respectively. The above solution was stored at 37 °C. The particle sizes of RSV-NPs and RSV-NPs@RBCm in fetal bovine serum were measured at 0, 2, 4, 6, 8, 12, 24 and 48 h. The particle size of RSV-NPs and RSV-NPs@RBCm in phosphate-buffered saline were measured at 0, 1st, 3rd, 5th, 7th, 9th, 11th and 13th day.

2.8. Nanoparticle uptake by HT29 and HCT116 Cells

The efficiency of uptake of nanoparticles by tumor cells was assessed using C6 instead of RSV as a fluorescent marker. Approximately 2×10^5 HT29, HCT116, and RAW cells were seeded in a confocal dish. Then replace the medium with RPMI 1640 containing C6-NPs or R-C6-NPs. After 4 h of incubation, the drug-containing was discarded, and the cell nuclei were dyed with DAPI for 30 min, and then observed under a confocal laser scanning microscope (CLSM).

2.9. *In vitro cytotoxicity studies*

HT29 and HCT116 cells were inoculated into 96-well plates at a density of 5×10^3 cells/well. After 24 h, treated with different concentrations of RSV, RSV-NPs, RSV-NPs@RBCm, and RSV-NPs@RBCm&iRGD respectively. 10 μl MTT working solution was put into every well and incubated for 4 h, and then dissolved formazan with dimethyl sulfoxide. After vibrating for 10 min, the absorbance at 492 nm was tested with a microplate reader.

2.10. *Colony formation assay*

HT29 cells were seeded in a 6-well plate at a density of 800 cells/well and treated with RSV, RSV-NPs, and RSV-NPs@RBCm separately for 48 h during the growth stage. After the treatment, the drug-containing medium was discarded and replaced with fresh RPMI 1640, and incubated for two weeks. Replaced the medium every three days. After 14 d, the cells grew into colonies and were fixed with 4% paraformaldehyde. Subsequently, it was dyed with 0.5% crystal violet, and the result was photographed with a camera. Calculate the colony numbers after each treatment for statistical analysis.

2.11. *Cell wound healing assay*

HT29 cells were put in a 6-well plate at a density of 6×10^5 cells/well. After 24 h, linear wounds were made on the bottom of the well using the p10 pipette tip. Then RSV, RSV-NPs, and RSV-NPs@RBCm were respectively added and incubated for 48 h. Finally, the cell images were taken under the microscope. The wound healing percentage is counted as follows:

$$\text{Wound healing percentage} = \frac{(0\text{ h scratch width} - 24\text{ h scratch width})}{(0\text{ h scratch width})} \times 100\%$$

2.12. *Cell migration assay*

In the cell migration experiment, 100 μl serum-free medium containing HT29 cells were put into the upper chamber, and 500 μl medium containing FBS was put in the lower chamber as a chemotactic factor. Different drugs were put into the upper chamber. After 48 h, cells that failed migrating through the membrane were wiped with a cotton bud. The cells were fixed with 4% paraformaldehyde for 20 min and then stained with 0.5% crystal violet for 15 min. The migration ratio is calculated as follows:

$$\text{Migration ratio (\%)} = \frac{\text{the number of cells penetrated the lower chamber}}{\text{total number of seeded cells}} \times 100\%$$

2.13. *Measurement of the mitochondrial membrane potential by JC-1*

The mitochondrial membrane potential (MMP) of the cell was tested by the JC-1 staining method. After HT29 cells were incubated with RSV, RSV-NPs, and RSV-NPs@RBCm for 8 h, the drug-containing medium was discarded. Then cells were incubated with JC-1 solution for 30 min. Then remove the JC-1 dye and wash twice with JC-1 buffer. Finally, CLSM was used to image the cells in the culture medium.

2.14. *Detection of intracellular ROS*

After treating HT29 cells with RSV, RSV-NPS, and RSV-NPs@RBCm for 4 h. The medium containing 10 μM DCFH-DA was used instead of the medium containing drugs to culture the cells for 40 min. Then the intracellular ROS level was recorded by CLSM.

2.15. *Malondialdehyde (MDA) assay*

MDA is the main indicator of lipid peroxidation. The protein concentration was tested and standardized according to the directions.

2.16. *Iron assay*

Intracellular chelate iron was determined using the fluorescent indicator phen green SK(#P14313) was got from Thermo Fisher, and its fluorescence could be reduced by iron quenching.

2.17. *Transmission electron microscopy (TEM)*

After treating HT29 cells with different administration groups for 48 h, the cells were collected by centrifugation. Cell fixation with 2.5% glutaraldehyde. The results were taken using TEM with different magnifications.

2.18. *Western-blot analysis*

The protein was collected from cells treated with RSV, RSV-NPs, and RSV-NPs@RBCm respectively for 48 h. The protein was isolated by SDS-PAGE and then transferred to the polyvinylidene fluoride (PVDF) membrane. The PVDF membrane was incubated with the primary antibody at 4 °C. The corresponding secondary antibody was combined with the primary antibody and then developed with a chemiluminescent horseradish peroxidase reagent. ChemiDoc imaging system (Tannon, China) was used to get results.

2.19. *In vivo evaluation*

The *in vivo* anti-tumor effects of RSV, RSV-NPs, RSV-NPs@RBCm, or RSV-NPs@RBCm&iRGD were evaluated on the HT29 xenograft model. Female nude mice were divided into 5 groups randomly, including the tumor model group (saline), free RSV group (RSV), RSV nanoparticles group (RSV-NPs), erythrocyte membrane-coated RSV nanoparticles group (RSV-NPs@RBCm), and RSV-NPs@RBCm and free iRGD group (RSV-NPs@RBCm&iRGD). Inoculating 5×10^6 cells into the left armpit of the mice. One week later, when the tumor size was 90 mm^3, mice in 5 groups were injected with physiological saline, RSV, RSV-NPs, RSV-NPs@RBCm, RSV-NPs@RBCm&iRGD (RSV and iRGD at a dose of 10 mg/kg) through the tail vein, respectively. The drug was given once a day at intervals for a total of seven injections. The body weight and tumor volume of the

mice were tested every other day. At last, all the mice were euthanized. The tumor, heart, liver, spleen, lung, and kidney were resected and immobilized in 4% paraformaldehyde overnight.

2.20. Histological analysis

Tumor, heart, liver, spleen, lung, and kidney sections were stained with hematoxylin and eosin (HE). Immunohistochemical antigens on slides were revealed and repaired by citric acid buffer boiling. The primary antibodies used in immunohistochemistry were as follows: Ki67 was diluted at 1:400, GPX4 (AF7020, Beyotime, China) at 1:400 dilution, SLC7A11/xCT (AF7992, Beyotime, China) was diluted 1:200. Finally, the sections were observed under an optical microscope.

2.21. Statistical analysis

The outcomes were measured as the mean ± standard deviation (SD). The significance of differences between groups was analyzed by an independent-sample t-test or a one-way analysis of variance (ANOVA). GraphPad Prism 8.0c software was used for statistical analysis. Semi-quantitative analysis of fluorescence images was carried out by Image J software. A probability level of $P < 0.05$ was regarded as significant.

3. Results and discussion

3.1. Ferroptosis contributed to RSV-induced cell death in colorectal cancer cells

The cytotoxicity of RSV against HT29 cells and HCT116 cells was measured by MTT assay (Fig. 1A). The results illustrated that RSV could dose-dependently inhibit the cell viability of HT29 and HCT116 cells. The IC_{50} values of RSV were 47.85±0.96 μg/ml and 23.65±3.21 μg/ml in HT29 and HCT116 cells, respectively ($P < 0.05$). In agreement with previous reports, RSV exhibits cytotoxic activity in colorectal cancer cells [36].

Ferrostatin-1 (fer-1) is a potent ferroptosis inhibitor that inhibits peroxidation reactions triggered by iron and traces lipid hydroperoxides in liposomes [37]. The ferroptosis inhibitor fer-1 was used to investigate whether RSV triggers ferroptosis in HT29 and HCT116 cells (Fig. 1B). When compared to free RSV, fer-1 effectively protected the cells from RSV-induced death at the equivalent dose ($P < 0.05$) representing the underlying role of ferroptosis in the cytotoxicity of RSV.

Moreover, unlike other forms of cell death, the feature of the ferroptosis is the appearance of smaller mitochondria and the reduction or vanishment of the mitochondria ridge [38]. It is obvious to locate the shrinkage of mitochondria volume and the disappearance of cristae in RSV treated HT29 cells, which demonstrates the induction of ferroptosis. On the contrary, co-administration of fer-1 significantly reversed the ferroptosis induced by RSV (Fig. 1C).

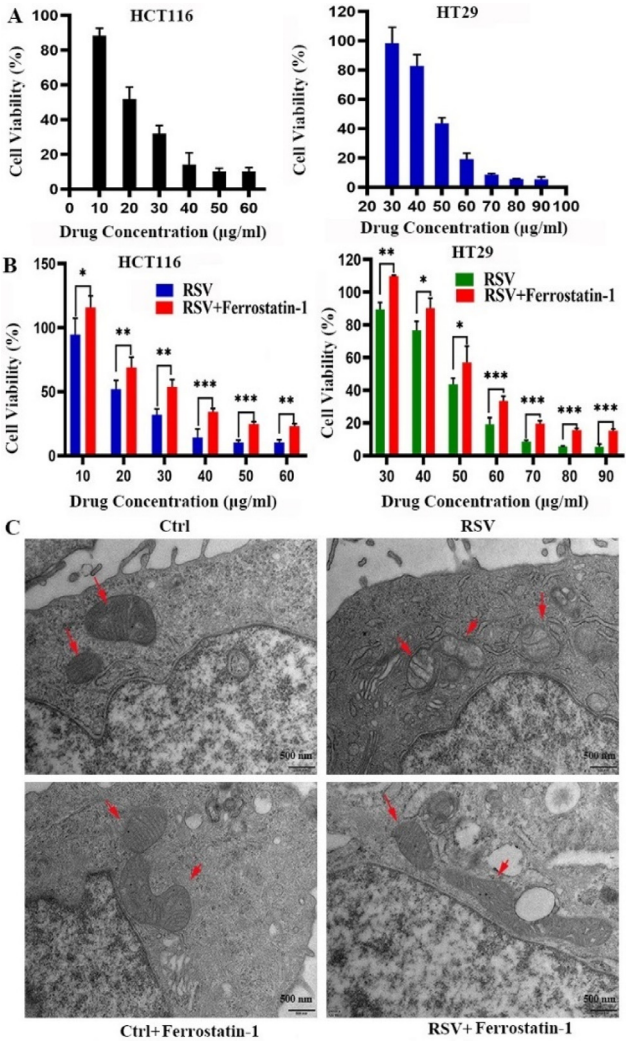

Fig. 1 – Ferroptosis contributes to RSV-induced cell death in colorectal cancer cells. (A) cell viability of HCT116 and HT29 cells when cultivated with RSV for 48 h. (B) Cell viability of HCT116 and HT29 cells treated with the indicated concentrations of RSV in the presence or absence of fer-1. (C) Characterization of ferroptosis by TEM in HT29 cells treated with RSV or fer-1. Mitochondria were marked with red arrows. Each point is displayed as mean ± SD ($n = 3$). * $P < 0.05$, ** $P < 0.01$, *** $P < 0.001$.

3.2. Preparation and characterization of nanoparticles

RSV-NPs@RBCm were synthesized as shown in Scheme 1. RSV was encapsulated into a core-shell structure of polymeric nanoparticles formed by mPEG-PCL (RSV-NPs) and then RSV-NPs were coated by a red blood cell membrane to generate RSV-loaded poly(ε-caprolactone)–poly(ethylene glycol) (PCL-PEG) nanoparticles with erythrocyte membrane (RSV-NPs@RBCm).

Fig. 2A, S1, and 2B showed that the particle size of RSV-NPs and RSV-NPs@RBCm were 141.32±0.43 nm and 160.91±0.63 nm, respectively, as tested by DLS. The zeta potential of RSV-NPs and RSV-NPs@RBCm were -12.56±0.76 mV and

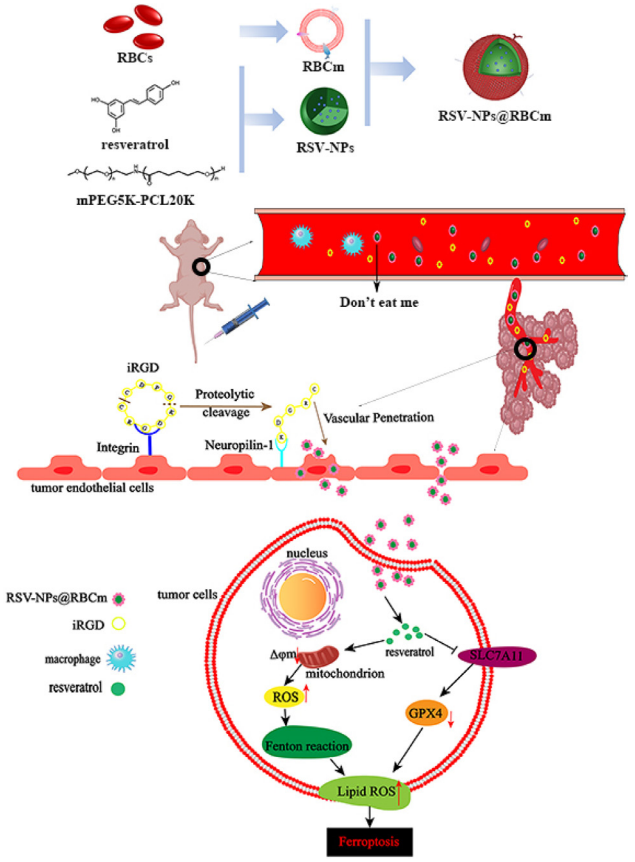

Scheme 1 – The synthesis procedure of the RSV-NPs@RBCm and the mechanism of cancer treatment by ferroptosis.

−31.64±0.91 mV, respectively (Fig. 2C). TEM visualization displayed that the size of RSV-NPs was about 120 nm and that of RSV-NPs@RBCm was about 140 nm (Fig. S4 and 2D), which was in accordance with the size from DLS. The drug loading content was up to 7.54% with the highest encapsulation efficiency of 45.25%. The enlarged size and the increased surface negative charge was mainly attributed to the successful fusion of RSV-NPs and RBC vesicles [39]. Fig. 2E showed that the membrane proteins were almost retained on the surface of RSV-NPs@RBCm. In addition, the expression of CD47 protein by SDS-PAGE was almost identical in both RSV-NPs and RSV-NPs@RBCm, demonstrating the successful wrap of the erythrocyte membrane around the surface of RSV-NPs (Fig. 2F). Nanoparticles were prepared by PCL-PEG-FITC, while red dye DiD was utilized to mark the erythrocyte membrane, followed by the coating of the pre-stained erythrocytes. After it was co-incubated with tumor cells, colocalization of red and green fluorescent signals was observed in the confocal microscope, which further indicated that the erythrocyte membrane has encapsulated the RSV-NPs (Fig. 2H).

In vitro stability test was performed in two kinds of medium (PBS and FBS). The size of RSV-NPs@RBCm remained almost unchanged with only slight enlargement in both medium. The particle size of RSV-NPs was also stable in FBS, but RSV-NPs showed a sudden increase in particle size on Day 8 in PBS. These results indicated that RSV-NPs@RBCm, compared to RSV-NPs, not only had superior serum stability but also guaranteed the possibility of long-term storage in PBS (Fig. S2 and S3).

Fig. 2G demonstrated the *in vitro* release of the nano-drug delivery systems at pH=6.5 and 7.4 at 37 °C. RSV was continuously released in 48 h with a burst release in the first several hours. There was a prominent difference between the release rate of pH 6.5 and pH 7.4, indicating a pH-responsive release pattern of both kinds of nanoparticles, which is due to an ester group structure -COO- in the PCL-PEG structure. In aqueous solution, water molecules can attack the ester group to break the bond and cause degradation. In acidic medium, the attack of water on the ester group is catalyzed, which accelerates the hydrolytic degradation of PCL-PEG [40,41]. Furthermore, the drug release rate of uncoated nanoparticles RSV-NPs was faster than that of RSV-NPs@RBCm. The reason may be that the coating of the erythrocyte membrane blocked the drug release to some extent.

3.3. *Cellular uptake of RSV-NPs@RBCm*

C6 was utilized as a fluorescent dye to track the uptake of nanospheres. Co-incubation for 4 h was enough for both kinds of colorectal cancer cells to uptake either C6-NPs or R-C6-NPs with green fluorescence, indicating the penetration of the nanoparticles into cancer cells (Fig. 3A and 3B). As shown in the semi-quantification analysis from Fig. 3D and 3E, the wrapping of the nanoparticles by the erythrocyte membrane did not influence the absorption by tumor cells ($P > 0.05$).

Most importantly, the uptake by macrophages was also investigated to assess the biocompatibility and the capability to escape immune cell clearance of RSV-NPs@RBCm. The green fluorescence in macrophages incubated with C6-NPs was significantly stronger than those cultured with R-C6-NPs (Fig. 3C). The absorption of C6-NPs and R-C6-NPs by macrophages was greatly different ($P < 0.05$) (Fig. 3F). Apparently, the erythrocyte membrane-encapsulated nanoparticles possessed the CD47 protein that expresses the "don't eat me" signal, making it possible to evade phagocytosis by immune cells [25].

3.4. *In vitro cytotoxicity and In vitro anti-metastasis of RSV-NPs@RBCm*

A safety test was performed in normal colorectal epithelial cell line NCM460. No obvious toxicity was observed in the NCM460 cell at a concentration as high as 400 μg/ml of blank nanoparticles (NPs@RBCm) (Fig. S5). Additionally, NPs@RBCm was also non-toxic to two kinds of cancer cell lines (HT29 and HCT116) (Fig. S6 and S7). Moreover, either free RSV or nanoparticle RSV (RSV-NPs and RSV-NPs@RBCm) led to dose-dependent cytotoxicity against both two colorectal cancer cell lines. Then, we used MTT method to detect the cytotoxicity of RSV, RSV-NPs and RSV-NPs@RBCm against colorectal cancer cells, such as HT29 and HCT116. Fig. 4A and 4B showed that the cell viability of HT29 and HCT116 cells under the treatment of different concentrations of RSV, RSV-NPs and RSV-NPs@RBCm for 48 h. The results showed that all the three

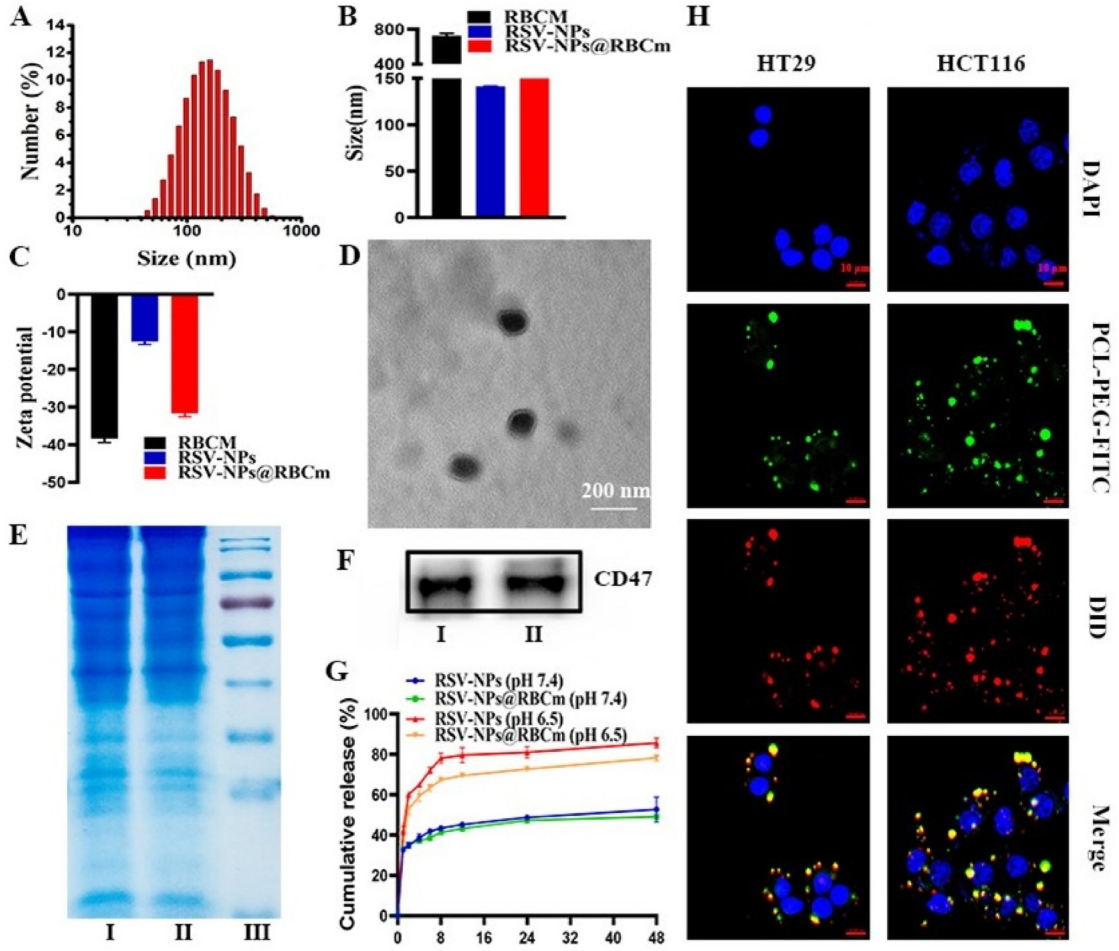

Fig. 2 – Characterization of RSV-NPs@RBCm. (A) Size distribution of RSV-NPs@RBCm measured by DLS. (B) The average particle size of RSV-NPs and RSV-NPs@RBCm, respectively. (C) Zeta potential of RSV-NPs, RSV-NPs@RBCm and RBCm. (D) TEM images of RSV-NPs@RBCm. (E) SDS-PAGE analysis of RBC-vesicles (I) and RSV-NPs@RBCm (II). (F) Western blotting analysis of CD47 in RBC-vesicles (I) and RSV-NPs@RBCm (II). (G) The RSV release from RSV-NPs and RSV-NPs@RBCm in PBS (pH = 6.5 and 7.4) *in vitro*. (H) CLSM of HT29 cells and HCT116 cells after incubation with RSV-NPs@RBCm by coating FITC-labeled RSV-NPs with DiD-labeled erythrocyte membrane for 1 h. The cell nucleus was stained with DAPI (blue), PCL-PEG was labeled with FITC (green), and the RBC membrane was labeled with DiD (red). Scale bars: 10 μm. Each point is displayed as mean ± SD ($n = 3$). * $P < 0.05$, ** $P < 0.01$, *** $P < 0.001$.

drug formulations had a dose-response effect on HT29 and HCT116 cells. The IC_{50} value of RSV-NPs was slightly higher than that of RSV because of the controlled release pattern. The IC_{50} of the RSV-NPs@RBCm was higher than that of the RSV-NPs group because of the outer shell of the erythrocyte membrane (Table S1).

As a valid way to evaluate the proliferative capacity of tumor cells, a clonogenic assay was designed to study the potential of cells in forming a large population with the reproductive ability [42]. In Fig. 4C and 4D, the number of colonies in RSV-NPs@RBCm treated groups was quite lower than in RSV treated group ($P < 0.05$), indicating the efficiency of RSV-NPs@RBCm to inhibit the proliferation of tumor cells. iRGD was co-administered with RSV-NPs@RBCm in the following *in vivo* study. So firstly, the combinational *in vitro* cytotoxicity was evaluated. As shown in Fig. S8 and S9, the addition of iRGD had no improvement in enhancing the cytotoxicity of RSV-NPs@RBCm, which was in accordance with previous studies [35,33]. Although the function of iRGD is increasing tumor vascular permeability by binding to integrin receptors, the combination of iRGD with RSV-NPs@RBCm showed little improvement in the cytotoxicity of tumor cells because of the absence of tumor vasculature *in vitro* [35].

A wound healing experiment and cell invasion experiment were adopted to investigate the inhibitory ability of nanoparticles on the invasion and migration influence of tumor cells. As shown in Fig. 4G and S10, RSV-NPs@RBCm significantly repressed the migration of HT29 cells when compared to free RSV ($P < 0.05$). Furthermore, a much more vigorous detainment in the ability of cell invasion was observed in the RSV-NPs@RBCm treated group (Fig. 4E and

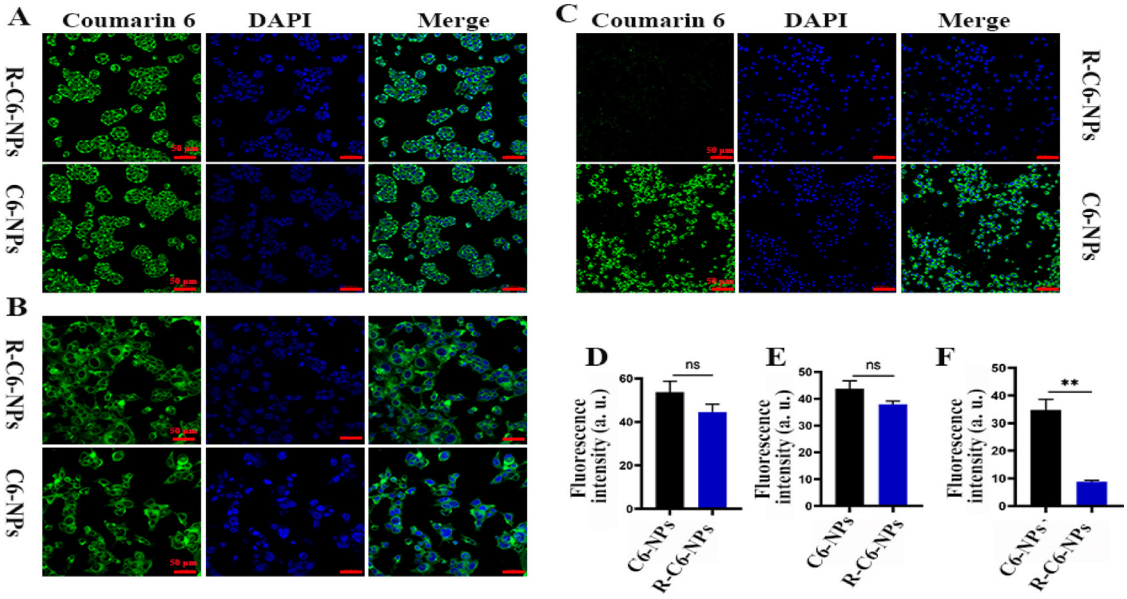

Fig. 3 – Intracellular uptake of RSV-NP and RSV-NPs@RBCm. Uptake of C6-NPs and R-C6-NPs in HT29 cells (A), HCT116 cells (B), and RAW264.7 cells (C). Quantification of the fluorescence intensity of HT29 cells (D), HCT116 cells (E), and RAW264.7 cells (F). Each point is displayed as mean ± SD ($n = 3$). ** $P < 0.01$, ns: no significant difference. The RSV-NP and RSV-NPs@RBCm were marked with C6.

4F). Therefore, results from the migration and invasion study suggested that RSV-NPs@RBCm exhibited a better ability to inhibit the invasion and migration due to the sustained release properties. The results of these *in vitro* cytotoxicity and anti-metastasis experiments demonstrated that RSV-NPs and RSV-NPs@RBCm groups were significantly better than the free RSV group in anti-tumor proliferation, invasion and metastasis. However, there was no significant difference between the RSV-NPs and RSV-NPs@RBCm groups, possibly because these experiments were *in vitro*, and the advantages of RSV-NPs@RBCm such as the long circulation effect and high biocompatibility could not be highlighted *in vitro*.

3.5. *The ferroptosis inducing effect of RSV-NPs@RBCm in colorectal cells*

Lipid peroxidation is a crucial checkpoint in ferroptosis. Fer-1 is a ferroptosis inhibitor because of the blockade of lipid peroxidation [37]. Accordingly, fer-1 was co-administered to study the role of RSV-NPs@RBCm in inducing ferroptosis. As shown in Fig. 5A and 5B, the dose-dependent cytotoxicity against both cancer cell lines was partially reversed by the co-administration of fer-1, revealing the role of ferroptosis in the cytotoxicity of both RSV-NPs and RSV-NPs@RBCm.

Ferroptosis is related to significant morphological changes in mitochondria, including mitochondrial disintegrated and cristae, decreased [43]. Mitochondrial morphological changes in HT29 cells treated with RSV-NPs and RSV-NPs@RBCm were visualized by TEM. The mitochondria of HT29 cells treated with RSV-NPs and RSV-NPs@RBCm showed reduced or even disappeared mitochondrial cristae when compared with the blank NPs treated group (Fig. 5C). Besides, co-administration of fer-1 counteracted the damage to mitochondria by the drug-loaded nanoparticles. Taken together, these results demonstrate that RSV-NPs@RBCm retained the ability of RSV by inducing ferroptosis in colorectal cancer cells.

3.6. *Mitochondrial dysfunction assay*

Ferroptosis is characterized by the dysfunction of mitochondria [44]. The intracellular red to green fluorescence ratio detected by JC-1 (5′,6,6′-tetrachloro-1,1′,3,3′-tetraethylbenzimidazolylcarbocyanine iodide) is a valid way to detect changes in mitochondrial membrane potential and monitor the function of mitochondria [45]. Normally, JC-1 forms polymers and emits red fluorescence in regular cells (Fig. 6A and 6H). However, damaged mitochondria are depolarized and the membrane potential is decreased, leading to the failure of polymer formation by JC-1 and lack of red fluorescence. Instead, monomers of JC-1 in the cytoplasm emit green fluorescence, suggesting the dysfunction of mitochondria. Fig. 6B-6D displayed the results that the ratio of red fluorescence to green fluorescence was significantly lower in HT29 cells with the treatment of RSV, RSV-NPs, and RSV-NPs@RBCm, indicating the reduction of MMP.

Mitochondrial dysfunction is an outcome of cellular oxidative damage, which is the result of the upregulation of oxidative stress [46]. The decrease of the electrochemical gradient ($\Delta\Psi m$) is the most important cause of the occurrence of endogenous mitochondrial damage [47]. Cells treated with free RSV and its formulations (RSV-NPs and RSV-NPs@RBCm) showed varying degrees of mitochondrial membrane potential changes, indicating the drug-induced

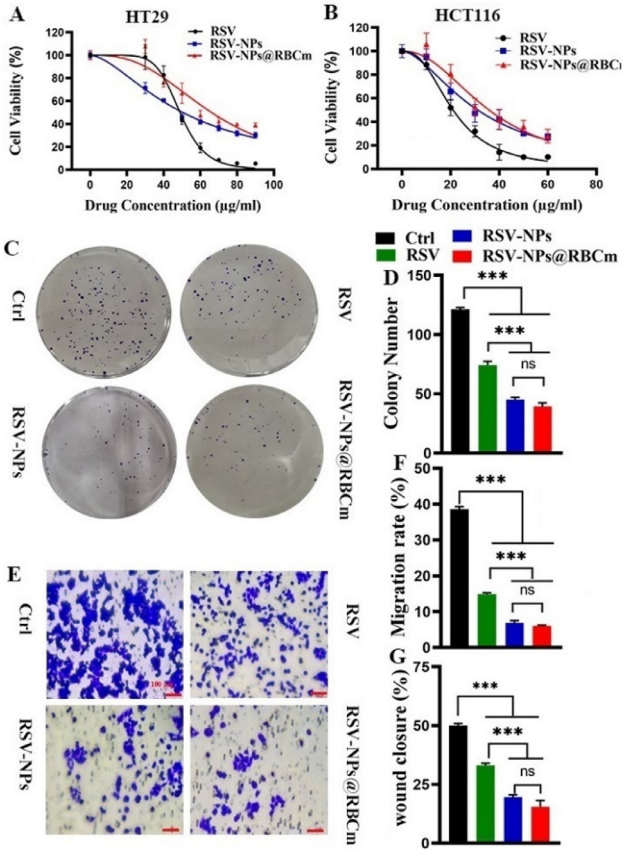

Fig. 4 – *In vitro* anticancer effects of RSV, RSV-NPs and RSV-NPs@RBCm. (A and B) Cell viabilities of HT29 and HCT116 cells upon 48 h treatment with RSV, RSV-NPs, and RSV-NPs@RBCm, respectively. (C) Clonogenicity assay of PBS, RSV, RSV-NPs and RSV-NPs@RBCm against HT29 cells for 48 h. (D) Quantitative analysis of colonies numbers. Each point is shown as mean ± SD (n = 3). *** $P < 0.001$, ns: no significant difference. (E) Migration assay of PBS, RSV, RSV-NPs and RSV-NPs@RBCm against HT29 cells for 48 h. (F) Quantitative analysis of the migration ratio. Each point is presented as mean ± SD (n = 3). *** $P < 0.001$, ns: no significant difference. (G) Quantitative analysis of wound healing. Each point is displayed as mean ± SD (n = 3). *** $P < 0.001$, ns: no significant difference.

mitochondrial damage, which is consistent with the results of cells in the drug-activated group shown in transmission electron microscopy ($P < 0.05$) (Fig. 6I). Most importantly, the pretreatment of a ferroptosis inhibitor fer-1 efficiently rescued the death of cells treated with RSV and the formulations, demonstrating a pivotal role of ferroptosis in RSV-induced cell death. (Fig. 6E-6G and 6J).

3.7. *Alteration of intracellular Fe^{2+} and Induction of ROS and MDA in colorectal cancer cells*

Iron-dependent mode of cell death is another key feature of ferroptosis. Phen Green SK, a heavy metal indicator, is often used to detect the concentration of Fe^{2+}. The fluorescence intensity of Phen Green SK has a negative relevance to the concentration of iron ions [48]. Fig. 7A and 7B showed that fer-1 did not affect the intracellular Fe^{2+}, while RSV and its formulations, especially RSV-NPs@RBCm significantly led to the attenuation of green fluorescence, indicating the induction of intracellular Fe^{2+} accumulation. Notably, co-treatment of fer-1 dramatically abolished the change of Fe^{2+} influx, suggesting the existence of ferroptosis in RSV-treated cells. Previous studies have demonstrated that there would be a large amount of Fe^{2+} accumulation in the cells with ferroptosis, and the accumulation of a large amount of Fe^{2+} also provides the basis for the Fenton reaction [49]. Our results were consistent with reports.

ROS is closely related to tumor cell growth and death. In ferroptosis, lipid peroxidation occurs mainly due to the reaction between ROS and polyunsaturated fatty acids (PUFAs) on lipid membranes [50]. To investigate the effect of ferroptosis from another point of view, the ROS-inducing effect of RSV and its formulations were evaluated by DCFH-DA [45]. It is obvious that RSV and its formulations were effective to induce ROS. RSV-NPs@RBCm showed an unparalleled ROS-inducing effect when compared with free RSV or RSV-NPs (Fig. 7C and 7D). As expected, the pretreatment of fer-1 led to a significant reversion of ROS generation, which consolidated that RSV-NPs@RBCm promoted the ferroptosis of colorectal cancer cells probably through excess intracellular ROS induction. We detected the content of ROS *in vivo* in the tumor of nude mice in different treatment groups by DCFH-DA. The results showed that free RSV, RSV-NPs, RSV-NPs@RBCm, and RSV-NPs@RBCm&iRGD groups could produce ROS, but more significant ROS production was observed in the three nano-formulation groups, which was consistent with the results of *in vitro* experiments (Fig. 9E).

One of the main traits of ferroptosis is lipid peroxidation, and MDA is the final product of lipid peroxidation [51]. MDA shows a key role in the induction of ferroptosis. Therefore, the changes in MDA levels were examined in cells with different treatments. As shown in Fig. 7F, MDA levels were elevated in all the drug-treated groups compared with the control group, while the pretreatment of fer-1 substantially attenuated the expression of MDA. These results suggested that both RSV and its formulations can induce ferroptosis through lipid peroxidation in colorectal cancer cells.

The expression of ferroptosis-related proteins was analyzed by Western blot. SLC7A11 and GPX4 are two of the most important proteins in the ferroptosis pathway [52]. As a negative regulator of ferroptosis, SLC7A11 is a part of the cystine/glutamate antiporter (System XC-), which can regulate ferroptosis by regulating cystine entering cells. When System XC- is inhibited, the cellular penetration of cystine is decreased with the blockade of GSH synthesis, eventually leading to ferroptosis [53]. In ferroptosis, GPX4 can convert lessened GSH to oxidized GSH and lipid hydroperoxide to its corresponding alcohol, when GPX4 is deactivated, the production of lipid peroxidation will increase and eventually lead to ferroptosis [54]. There was a prominent decrease in the expression of SLC7A11 and GPX4 in cells processed with RSV and its formulations. Moreover, RSV-NPs@RBCm considerably strengthened the induction of ferroptosis compared to free RSV or RSV-NPs. Similar to the MDA assay, pretreatment of fer-1 partially reversed the expression of SLC7A11 and

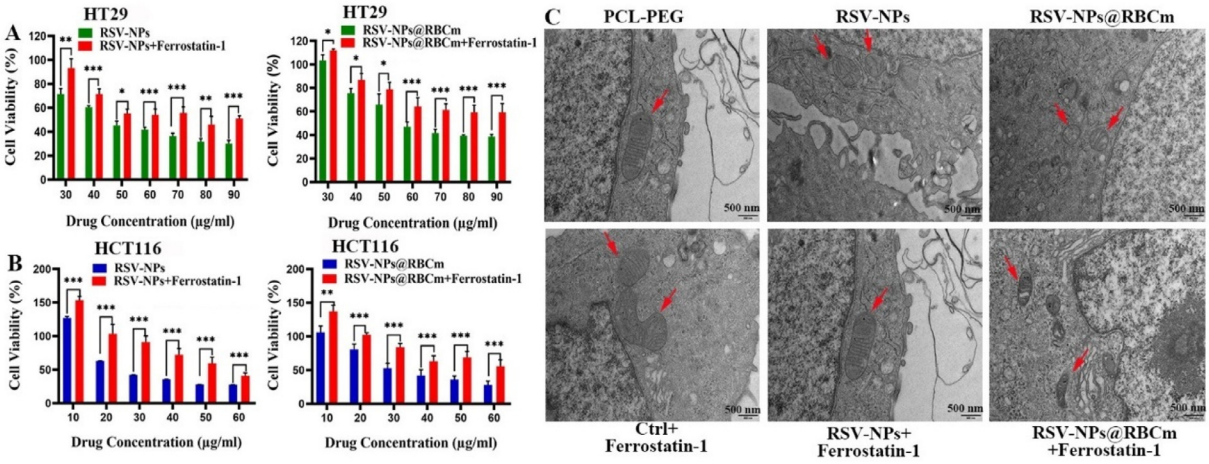

Fig. 5 – Ferroptosis inducing effect of RSV formulations. (A) cell viability of HT29 cells when incubated with RSV formulations with or without the presence of fer-1. (B) cell viability of HCT116 cells when incubated with RSV formulations with or without the presence of fer-1 for 48 h. (C) Characterization of ferroptosis by TEM in HT29 cells treated with RSV formulations or fer-1. Mitochondria were marked with red arrows. Results are displayed as the mean ± SD ($n = 3$). (*$P < 0.05$, ** $P < 0.01$, *** $P < 0.001$.)

GPX4, thereby mitigating the initiation and progression of ferroptosis (Fig. 7E).

3.8. *Pharmacokinetics and biodistribution of RSV-NPs@RBCm&iRGD*

We further investigated the pharmacokinetics of free RSV, RSV-NPs, RSV-NPs@RBCm, and RSV-NPs@RBCm&iRGD in mice. The results displayed that RSV-NPs@RBCm and RSV-NPs@RBCm&iRGD groups retained more of the drug in the circulating blood at 48 h compared to other groups (Fig. S14). This indicated that RSV-NPs@RBCm and RSV-NPs@RBCm&iRGD could escape the phagocytosis of immune cells because of the biomimetic erythrocyte membrane, so they have longer blood circulation.

We also evaluated the *in vivo* distribution of nanoparticles in mice. Fig. 8A showed fluorescence images of mice at various time points following tail vein injection of saline, free DiR, DiR-NPs, DiR-NPs@RBCm, and DiR-NPs@RBCm&iRGD. The results demonstrated that the DiR-NPs@RBCm and DiR-NPs@RBCm&iRGD groups significantly increased tumor accumulation at 48 h. After 48 h, the main organs and tumor tissues were removed for *ex vivo* fluorescence imaging. Fig. 8B and 8C showed that the fluorescence signal of the tumor in the fluorescence intensity of DiR-NPs@RBCm&iRGD group was significantly higher than that of the other groups ($P < 0.05$). It was not only due to the long circulation effect of erythrocyte membrane, but also related to the co-delivery of iRGD increasing the permeability of tumor blood vessels, thereby increasing the accumulation of drugs in tumors.

To further determined whether co-delivery of the nanoparticles with iRGD increased the distribution of the nanoparticles in the tumor, the tumor tissues from the *in vivo* biodistribution experiment were removed for cryo-section. Fig. 8D displayed that the DiR-NPs@RBCm&iRGD group significantly promoted the penetration of drug into tumor parenchyma. Our result was similar to that reported in previous paper, indicating that coadministration with iRGD can enhance the accumulation and permeation of nanoparticles into tumors [35].

3.9. *In vivo Antitumor and biosafety assessment*

As shown in Fig. 9A, tumors grew rapidly in the physiological saline group, and the tumor increased to more than 700 mm^3 14 d after inoculation. Mice treated with RSV and its formulations showed a slower growth rate of the tumor when compared with the saline group. It is noteworthy that the combinational use of RSV-NPs@RBCm and iRGD dramatically delayed the tumor growth than the single administration of RSV-NPs@RBCm ($P < 0.05$), demonstrating the amplification of the anticancer effect by cooperating with the enhanced tumor targeting and penetration. When the experiment was finished, the mice were euthanized, and then tumors and organs were resected. The average tumor weight of the RSV-NPs@RBCm&iRGD group was the lightest among all groups (Fig. 9B) ($P < 0.05$). A photograph of nude mice tumors was taken out on the 15th day as shown in Fig. 9C, tumors in the RSV-NPs@RBCm&iRGD group were visibly smaller than in other groups.

The results above showed that the RSV-NPs@RBCm&iRG group achieved an excellent antitumor ability. The advantages of the RSV-NPs@RBCm&iRG group lie in the following points. Firstly, the sustained release of the nanoparticles could deliver its antitumor efficacy constantly. And secondly, nanoparticles were coated by the erythrocyte membrane, allowing them to escape phagocytosis by immune cells, circulate longer in

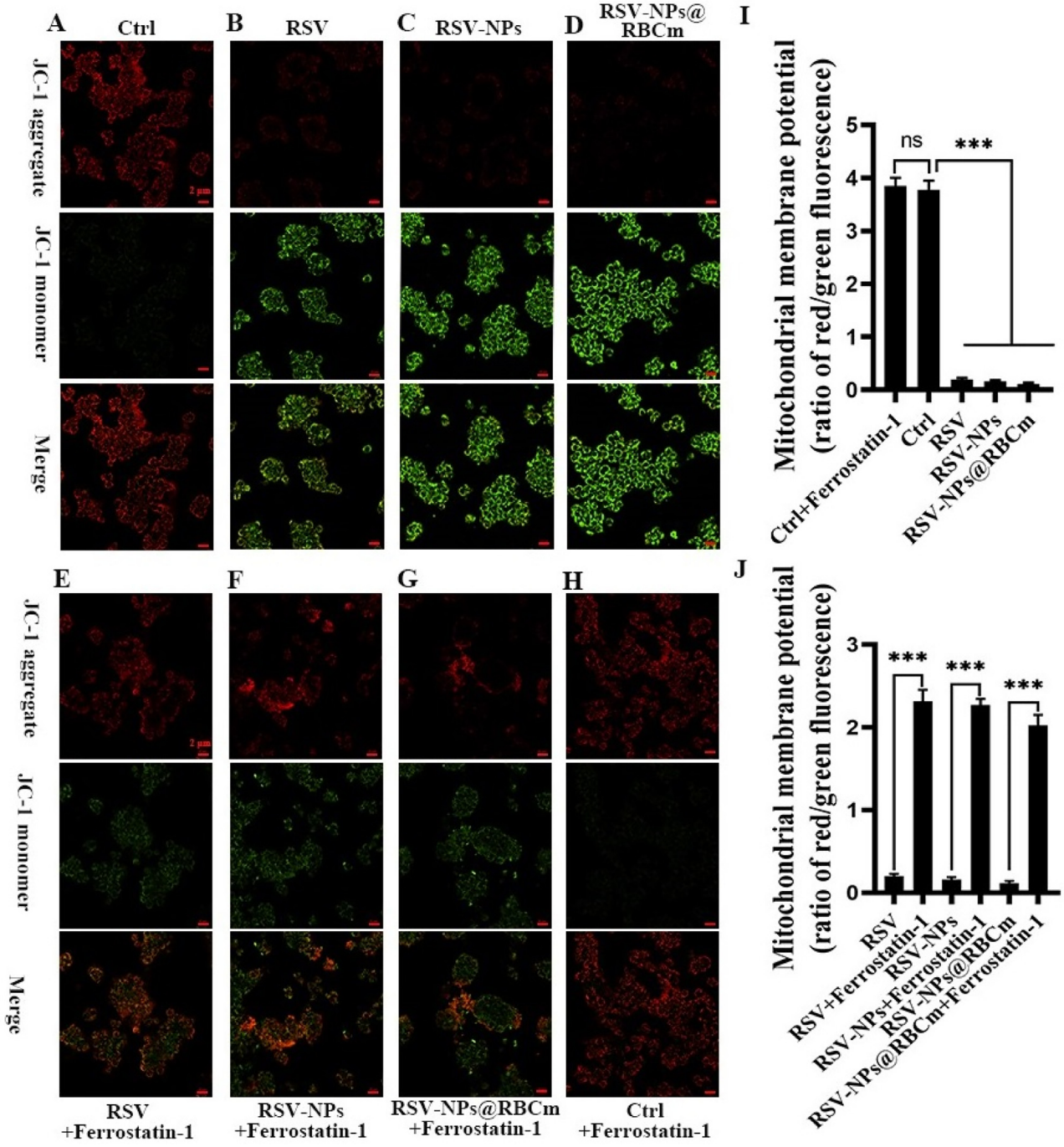

Fig. 6 – The confocal fluorescent image of JC-1 dyes with different treatments in HT29 cells. Detection of mitochondrial membrane potential (MMP, $\Delta\psi$) in colorectal cancer cells. Measurement of MMP was performed by labeling with JC-1. MMP measurement on HT29 cells after incubation with control (A), RSV (B), RSV-NPs (C), RSV-NPs@RBCm (D). The ferroptosis inhibitor fer-1was used to pretreat cells for 1 h. MMP measurement on pre-conditioned HT29 cells after incubation with RSV (E), RSV-NPs (F), RSV-NPs@RBCm (G), control (H). Quantification data of MMP in HT29 cells (I and J). Each point is displayed as mean ± SD ($n = 3$). (*$P < 0.001$, ns: no significant difference.)**

the body, and then remain in the blood for a longer time, so they can accumulate more in the tumor site. Last but not least, due to the rich vascularity of solid tumors, combined with iRGD peptide administration can remarkably enhance the *in vivo* efficacy of RSV-NPs@RBCm for colorectal cancer. Previous studies have demonstrated that co-delivery of iRGD can increase tumor delivery effects of nanomedicine for cancer [35]. The RGD combined with the tumor site, then

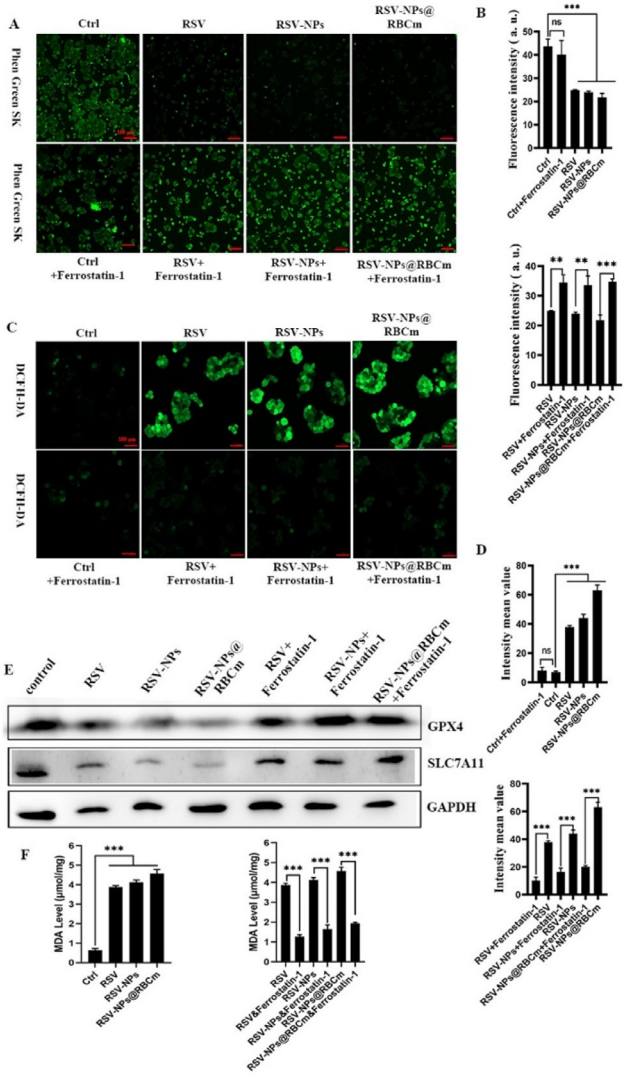

Fig. 7 – RSV, RSV-NPs, and RSV-NPs@RBCm induced the ROS-mediated ferroptosis of colorectal cancer cells. (A) Intracellular chelate iron in HT29 cells treated with equivalent doses of free RSV, RSV-NPs, and RSV-NPs@RBCm with or without fer-1 was measured by the fluorescent indicator Phen Green™ SK (green). (B) Quantification of Phen Green™ SK staining of HT29 cells treated with free RSV, RSV-NPs, and RSV-NPs@RBCm with or without fer-1 for 4 h. (C) Images of HT29 cells dyed by DCFH-DA treated with equivalent dosages of free RSV, RSV-NPs, and RSV-NPs@RBCm with or without fer-1. (D) Quantification of DCFH-DA staining of HT29 cells dealt with free RSV, RSV-NPs, and RSV-NPs@RBCm with or without fer-1 for 4 h. (E) The expression of several key ferroptosis regulators was examined by western blotting. GAPDH was used as an internal control. (F) Intracellular MDA levels in HT29 cells treated with free RSV, RSV-NPs, and RSV-NPs@RBCm with or without fer-1. Each point is displayed as mean ± SD ($n = 3$). ($P < 0.01$, *** $P < 0.001$, ns: no significant difference, n=3.)**

CendR irritated vascular permeability, and finally promoted effective transport of the co-administered nanoparticles from tumor vessels to tumor parenchyma [55].

Then, the tumor tissues of different treatment groups were sectioned and stained with HE to study the histological morphology (Fig. 9D). The expression of Ki-67, GPX4, and SLC7A11 by immunohistochemical staining was also investigated. The ki-67 index is commonly used to assess cell proliferation. A higher percentage of Ki-67 positive cells indicates more rapid tumor growth and a worse prognosis [14]. As shown in Fig. 9D, the expression of Ki-67 was obviously decreased after effective drug therapy with all the treatment groups, especially RSV-NPs@RBCm&iRGD. This result reflected the good ability of RSV-NPs@RBCm&iRGD to inhibit tumor cell proliferation *in vivo*. Moreover, the expression of the ferroptosis-related molecule SLC7A11 and GPX4 was noticeably weakened in tumors treated with RSV-NPs@RBCm&iRGD, indicating the most robust restriction of ferroptosis (Fig. 9D). These results suggested that RSV-NPs@RBCm can effectively induce ferroptosis in cells, resulting in a powerful antitumor effect.

Biosafety is of essential importance in quality control for any drug. The biosafety of NPs@RBCm&iRGD was evaluated in our preliminary *in vivo* experiments. There was no distinction in the body weight, tumor volume, and tumor weight of mice, between the NPs@RBCm&iRGD group and saline group, demonstrating that polymers, RBCm, and iRGD had no obvious toxicity in animals and had no inhibitory effect on tumor growth (Fig. S11-13). Then, a series of biosafety studies were proceeded to assess the biosafety in the treatment group. The histopathology of the heart, liver, spleen, lung, and kidney of mice in different treatment groups was examined after being stained with H&E. As displayed in Fig. 10C, compared with the saline section, no obvious abnormality was shown in the stained organ section of the drug treatment groups, indicating the good security of RSV, RSV-NPs, RSV-NPs@RBCm, and RSV-NPs@RBCm&iRGD. In addition, there was no significant discrepancy in the weight of mice in each treatment group, which suggested that drug treatment would not lead to the weight loss of mice (Fig. 10A and 10B) ($P < 0.05$). Therefore, RSV-NPs@RBCm&iRGD could not only enhance the antitumor effect of RSV but also improve the biosafety of RSV.

4. Conclusion

To sum up, our study proved for the first time that RSV could induce ferroptotic cell death in colorectal cancer through initiating lipid peroxidation and suppressing the expression of SLC7A11 and GPX4. A biomimetic nanocarrier was developed by coating RSV-loaded poly(ε-caprolactone)–poly(ethylene glycol) (PCL-PEG) nanoparticles with erythrocyte membrane (RSV-NPs@RBCm). Encapsulation in the nano-delivery system not only improves the poor water solubility of RSV but also makes it escape from the monitor of immune cells

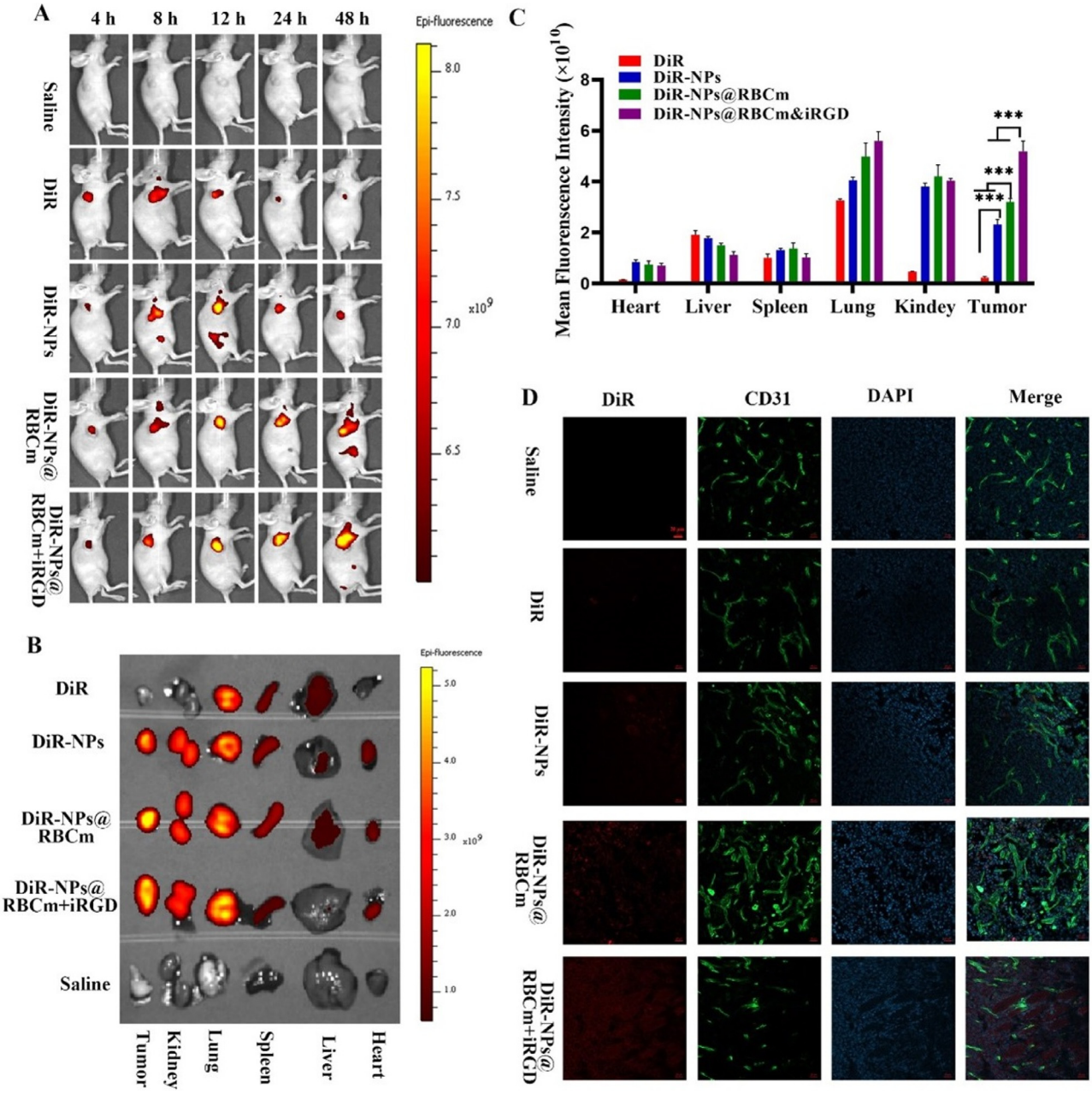

Fig. 8 – *In vivo* biodistribution of RSV-NPs@RBCm&iRGD. (A) Representative *in vivo* images of mice at different times after different administrations. (B) *Ex vivo* fluorescence images of heart, liver, spleen, lung, kidney, and tumor at 48 h after injection. (C) Quantitative analysis of the DiR fluorescence intensity of the major organs and tumor tissues at 48 h after different administrations. (D) Immunofluorescence images of tumor cryo-section in saline, free DiR, DiR-NPs, DiR-NPs@RBCm, and DiR-NPs@RBCm&iRGD groups at 48 h post-injection. The tumor blood vessels were stained with CD31 antibody (green), nanoparticles were labeled with DiR (red), and the tumor cell nucleus was labeled with DAPI (blue). Scale bar: 20 μm. Each point is displayed as mean ± SD ($n = 3$). *** $P < 0.001$.

and enhances its biocompatibility. *In vivo* experiments also showed that the RSV-NPs@RBCM co-administration delivery system with iRGD possessed obvious advantages compared with iRGD-free nanoparticles, including the enhancement of tumor penetration and anti-tumor activity. Combined with the *In vitro* and *in vivo* experiments of this study, it is demonstrated that an RSV-NPs@RBCM co-administration delivery system with iRGD could be a promising drug delivery method for the therapeutics of colorectal cancer.

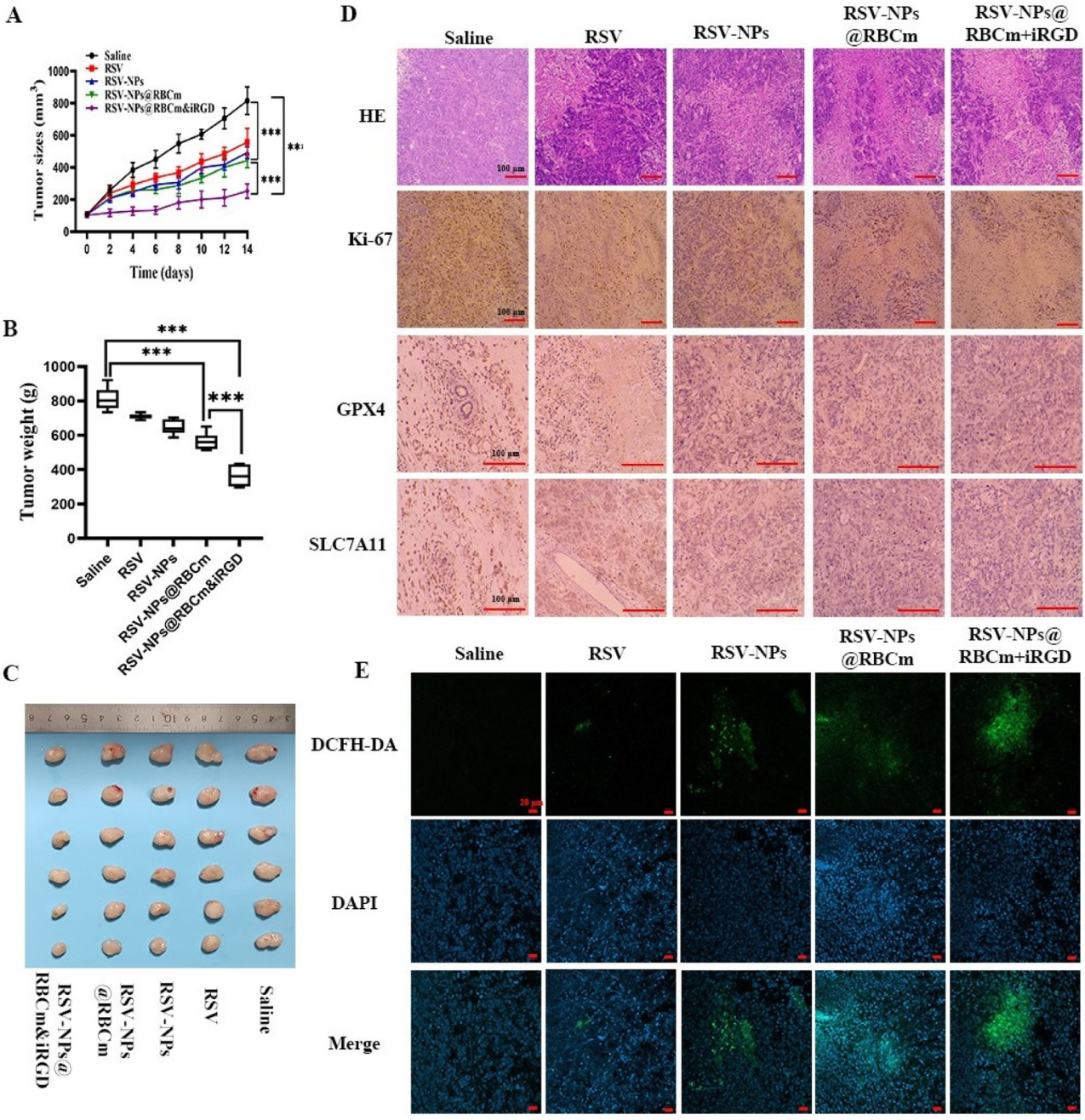

Fig. 9 – *In vivo* antitumor effect of RSV-NPs@RBCm&iRGD. (A) Change of tumor size of mice after treatment with saline, RSV, RSV-NPs, RSV-NPs@RBCm, or RSV-NPs@RBCm&iRGD. (B) Tumor weight of the removed tumor after mouse euthanasia. (C) Representative photograph of the excised tumor of mice after different treatments. (D) HE staining and immunohistochemical staining of Ki-67, GPX4, and SLC7A11 expression in tumor tissue sections from mice treated with different drug formulations. (E) Fluorescent images of ROS from *in vivo* tumors after intravenous injection through the tail vein of saline, free RSV, RSV-NPs, RSV-NPs@RBCm and RSV-NPs@RBCm&iRGD. Scale bar: 20 μm. Each point is displayed as mean ± SD ($n = 3$). *** $P < 0.001$.

Conflicts of interest

The authors report no conflicts of interest. The authors alone are responsible for the content and writing of this article.

Acknowledgments

This work was supported by the National Natural Science Foundation of China (81773211, 81871942, 82073308, and

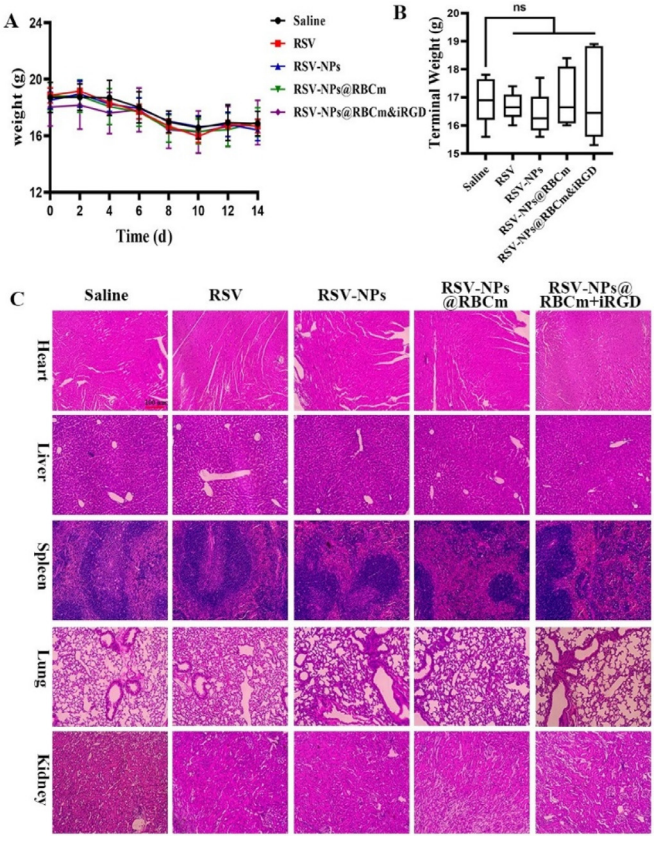

Fig. 10 – *In vivo* toxicity of RSV-NPs@RBCm&iRGD (A) The body weight of HT29 tumor-bearing mice in each treatment group. (B) The terminal body weight of tumor-bearing mice in each treatment group. (C) HE staining of heart, liver, spleen, lung, and kidney. Each point is presented as mean ± SD ($n = 6$). Scale bars, 100 μm. ns means no significance

81672411), the High-level startup fund of Nanjing Medical University (KY109RC2019010), and the Natural Science Foundation of Jiangsu Province (BK20201086).

Supplementary materials

Supplementary material associated with this article can be found, in the online version, at doi:10.1016/j.ajps.2022.07.006.

REFERENCES

[1] Dekker E, Tanis PJ, Vleugels JLA, Kasi PM, Wallace MB. Colorectal cancer. Lancet 2019;394(10207):1467–80.
[2] Siegel RL, Miller KD, Fuchs HE, Jemal A. Cancer statistics, 2022. CA Cancer J Clin 2022;72(1):7–33.
[3] Cassidy S, Syed BA. Colorectal cancer drugs market. Nat Rev Drug Discov 2017;16(8):525–6.
[4] Xia Y, Liu S, Li C, Ai Z, Shen W, Ren W, et al. Discovery of a novel ferroptosis inducer-talaroconvolutin A-killing colorectal cancer cells *in vitro* and *in vivo*. Cell Death Dis 2020;11(11):988.
[5] Wang Z, Ding Y, Wang X, Lu S, Wang C, He C, et al. Pseudolaric acid B triggers ferroptosis in glioma cells via activation of Nox4 and inhibition of xCT. Cancer Lett 2018;428:21–33.
[6] Cao JY, Dixon SJ. Mechanisms of ferroptosis. Cell Mol Life Sci 2016;73(11-12):2195–209.
[7] Huang S, Cao B, Zhang J, Feng Y, Wang L, Chen X, et al. Induction of ferroptosis in human nasopharyngeal cancer cells by cucurbitacin B: molecular mechanism and therapeutic potential. Cell Death Dis 2021;12(3):237.
[8] Latunde-Dada GO. Ferroptosis: Role of lipid peroxidation, iron and ferritinophagy. Biochim Biophys Acta Gen Subj 2017;1861(8):1893–900.
[9] Dixon SJ, Lemberg KM, Lamprecht MR, Skouta R, Zaitsev EM, Gleason CE, et al. Ferroptosis: an iron-dependent form of nonapoptotic cell death. Cell 2012;149(5):1060–72.
[10] Wei R, Zhao Y, Wang J, Yang X, Li S, Wang Y, et al. Tagitinin C induces ferroptosis through PERK-Nrf2-HO-1 signaling pathway in colorectal cancer cells. Int J Biol Sci 2021;17(11):2703–17.
[11] Sun Q, He M, Zhang M, Zeng S, Chen L, Zhao H, et al. Traditional chinese medicine and colorectal cancer: implications for drug discovery. Front Pharmacol 2021;12:685002.
[12] Rejhová A, Opattová A, Čumová A, Slíva D, Vodička P. Natural compounds and combination therapy in colorectal cancer treatment. Eur J Med Chem 2018;144:582–94.
[13] Qi X, Yang N, Luo Y, Jia X, Zhao J, Feng X, et al. Resveratrol as a plant type antioxidant modifier for polysulfone membranes to improve hemodialysis-induced oxidative stress. Mater Sci Eng C Mater Biol Appl 2021;123:111953.
[14] Harikumar KB, Kunnumakkara AB, Sethi G, Diagaradjane P, Anand P, Pandey MK, et al. Resveratrol, a multitargeted agent, can enhance antitumor activity of gemcitabine *in vitro* and in orthotopic mouse model of human pancreatic cancer. Int J Cancer 2010;127(2):257–68.
[15] Du Q, Hu B, An HM, Shen KP, Xu L, Deng S, et al. Synergistic anticancer effects of curcumin and resveratrol in Hepa1-6 hepatocellular carcinoma cells. Oncol Rep 2013;29(5):1851–8.
[16] Ursini F, Maiorino M. Lipid peroxidation and ferroptosis: the role of GSH and GPx4. Free Radic Biol Med 2020;152:175–85.
[17] Bano S, Ahmed F, Khan F, Chaudhary SC, Samim M. Enhancement of the cancer inhibitory effect of the bioactive food component resveratrol by nanoparticle based delivery. Food Funct 2020;11(4):3213–26.
[18] Li Y, Liu J, Liu B, Tomczak N. Highly emissive PEG-encapsulated conjugated polymer nanoparticles. Nanoscale 2012;4(18):5694–702.
[19] Yuan H, Chen CY, Chai GH, Du YZ, Hu FQ. Improved transport and absorption through gastrointestinal tract by PEGylated solid lipid nanoparticles. Mol Pharm 2013;10(5):1865–73.
[20] Magarkar A, Karakas E, Stepniewski M, Róg T, Bunker A. Molecular dynamics simulation of PEGylated bilayer interacting with salt ions: a model of the liposome surface in the bloodstream. J Phys Chem B 2012;116(14):4212–19.
[21] Song LY, Ahkong QF, Rong Q, Wang Z, Ansell S, Hope MJ, et al. Characterization of the inhibitory effect of PEG-lipid conjugates on the intracellular delivery of plasmid and antisense DNA mediated by cationic lipid liposomes. Biochim Biophys Acta 2002;1558(1):1–13.
[22] Zhang P, Sun F, Liu S, Jiang S. Anti-PEG antibodies in the clinic: current issues and beyond PEGylation. J Control Rel 2016;244(Pt B):184–93.
[23] Ishida T, Maeda R, Ichihara M, Irimura K, Kiwada H. Accelerated clearance of PEGylated liposomes in rats after repeated injections. J Control Rel 2003;88(1):35–42.
[24] Villa CH, Anselmo AC, Mitragotri S, Muzykantov V. Red blood cells: supercarriers for drugs, biologicals, and nanoparticles and inspiration for advanced delivery systems. Adv Drug Deliv Rev 2016;106(Pt A):88–103.

[25] Li R, He Y, Zhang S, Qin J, Wang J. Cell membrane-based nanoparticles: a new biomimetic platform for tumor diagnosis and treatment. Acta Pharm Sin B 2018;8(1):14–22.
[26] Xia Q, Zhang Y, Li Z, Hou X, Feng N. Red blood cell membrane-camouflaged nanoparticles: a novel drug delivery system for antitumor application. Acta Pharm Sin B 2019;9(4):675–89.
[27] Han X, Wang C, Liu Z. Red blood cells as smart delivery systems. Bioconjug Chem 2018;29(4):852–60.
[28] Rao L, Bu LL, Xu JH, Cai B, Yu GT, Yu X, et al. Red blood cell membrane as a biomimetic nanocoating for prolonged circulation time and reduced accelerated blood clearance. Small 2015;11(46):6225–36.
[29] Tietjen GT, Saltzman WM. Nanomedicine gets personal. Sci Transl Med 2015;7(314):314fs47.
[30] Danhier F. To exploit the tumor microenvironment: Since the EPR effect fails in the clinic, what is the future of nanomedicine? J Control Rel 2016;244(Pt A):108–21.
[31] Wang T, Wang D, Liu J, Feng B, Zhou F, Zhang H, et al. Acidity-triggered ligand-presenting nanoparticles to overcome sequential drug delivery barriers to tumors. Nano Lett 2017;17(9):5429–36.
[32] Kang S, Lee S, Park S. iRGD peptide as a tumor-penetrating enhancer for tumor-targeted drug delivery. Polymers (Basel) 2020;12(9):1906.
[33] Alberici L, Roth L, Sugahara KN, Agemy L, Kotamraju VR, Teesalu T, et al. De novo design of a tumor-penetrating peptide. Cancer Res 2013;73(2):804–12.
[34] Sun L, Xiong Z, Shen F, Wang Z, Liu Z. Biological membrane derived nanomedicines for cancer therapy. Sci China Chem 2021;64:719–33.
[35] Zhong Y, Su T, Shi Q, Feng Y, Tao Z, Huang Q, et al. Co-administration of iRGD enhances tumor-targeted delivery and anti-tumor effects of paclitaxel-loaded PLGA nanoparticles for colorectal cancer treatment. Int J Nanomed 2019;14:8543–60.
[36] Honari M, Shafabakhsh R, Reiter RJ, Mirzaei H, Asemi Z. Resveratrol is a promising agent for colorectal cancer prevention and treatment: focus on molecular mechanisms. Cancer Cell Int 2019;19:180.
[37] Miotto G, Rossetto M, Di Paolo ML, Orian L, Venerando R, Roveri A, et al. Insight into the mechanism of ferroptosis inhibition by ferrostatin-1. Redox Biol 2020;28:101328.
[38] Xie Y, Hou W, Song X, Yu Y, Huang J, Sun X, et al. Ferroptosis: process and function. Cell Death Differ 2016;23(3):369–79.
[39] Gao M, Liang C, Song X, Chen Q, Jin Q, Wang C, et al. Erythrocyte-membrane-enveloped perfluorocarbon as nanoscale artificial red blood cells to relieve tumor hypoxia and enhance cancer radiotherapy. Adv Mater 2017;29(35):1–7.
[40] Castilla-Cortazar I, Mas-Estelles J, Meseguer-Duenas JM, Ivirico JLE, Mari B, Vidaurre A. Hydrolytic and enzymatic degradation of a poly(ε-caprolactone) network. Polym Degrad Stab 2012;97(8):1241–8.
[41] Wei X, Gong C, Gou M, Fu S, Guo Q, Shi S, et al. Biodegradable poly(epsilon-caprolactone)-poly(ethylene glycol) copolymers as drug delivery system. Int J Pharm 2009;381(1):1–18.
[42] Franken NA, Rodermond HM, Stap J, Haveman J, van Bree C. Clonogenic assay of cells *in vitro*. Nat Protoc 2006;1(5):2315–19.
[43] Gao M, Yi J, Zhu J, Minikes AM, Monian P, Thompson CB, et al. Role of mitochondria in ferroptosis. Mol Cell 2019;73(2) 354–63.e3.
[44] Hao J, Zhang W, Huang Z. Bupivacaine modulates the apoptosis and ferroptosis in bladder cancer via phosphatidylinositol 3-kinase (PI3K)/AKT pathway. Bioengineered 2022;13(3):6794–806.
[45] Smiley ST, Reers M, Mottola-Hartshorn C, Lin M, Chen A, Smith TW, et al. Intracellular heterogeneity in mitochondrial membrane potentials revealed by a J-aggregate-forming lipophilic cation JC-1. Proc Natl Acad Sci USA 1991;88(9):3671–5.
[46] Luo Y, Ma J, Lu W. The significance of mitochondrial dysfunction in cancer. Int J Mol Sci 2020;21(16):5598.
[47] Li X, Yu N, Li J, Bai J, Ding D, Tang Q, et al. Novel "carrier-free" nanofiber codelivery systems with the synergistic antitumor effect of paclitaxel and tetrandrine through the enhancement of mitochondrial apoptosis. ACS Appl Mater Interfaces 2020;12(9):10096–106.
[48] Hirayama T, Nagasawa H. Chemical tools for detecting Fe ions. J Clin Biochem Nutr 2017;60(1):39–48.
[49] Chen P, Wu Q, Feng J, Yan L, Sun Y, Liu S, et al. Erianin, a novel dibenzyl compound in Dendrobium extract, inhibits lung cancer cell growth and migration via calcium/calmodulin-dependent ferroptosis. Signal Transduct Target Ther 2020;5(1):51.
[50] Wang H, Cheng Y, Mao C, Liu S, Xiao D, Huang J, et al. Emerging mechanisms and targeted therapy of ferroptosis in cancer. Mol Ther 2021;29(7):2185–208.
[51] Yang WS, Stockwell BR. Ferroptosis: death by lipid peroxidation. Trends Cell Biol 2016;26(3):165–76.
[52] Lei G, Zhang Y, Hong T, Zhang X, Liu X, Mao C, et al. Ferroptosis as a mechanism to mediate p53 function in tumor radiosensitivity. Oncogene 2021;40(20):3533–47.
[53] Koppula P, Zhang Y, Zhuang L, Gan B. Amino acid transporter SLC7A11/xCT at the crossroads of regulating redox homeostasis and nutrient dependency of cancer. Cancer Commun (Lond) 2018;38(1):12.
[54] Friedmann Angeli JP, Schneider M, Proneth B, Tyurina YY, Tyurin VA, Hammond VJ, et al. Inactivation of the ferroptosis regulator Gpx4 triggers acute renal failure in mice. Nat Cell Biol 2014;16(12):1180–91.
[55] Wang K, Zhang X, Liu Y, Liu C, Jiang B, Jiang Y. Tumor penetrability and anti-angiogenesis using iRGD-mediated delivery of doxorubicin-polymer conjugates. Biomaterials 2014;35(30):8735–47.